MDPI

Article

Investigation of the Dynamic Strain Aging Effect in Austenitic Weld Metals by 3D-DIC

Amke Lescur [1,2,*] , **Erich Stergar** [1] , **Jun Lim** [1] , **Stijn Hertelé** [2] and **Roumen H. Petrov** [2,3]

1   Belgian Nuclear Research Centre (SCK CEN), 2400 Mol, Belgium
2   Department of Electromechanical Systems & Metal Engineering, Ghent University, 9000 Ghent, Belgium
3   Department of Materials Science and Engineering, Delft University of Technology,
    2628 CD Delft, The Netherlands
*   Correspondence: amke.lescur@sckcen.be

Abstract: Austenitic stainless steels similar to type AISI 316L are widely used structural materials in current and future nuclear reactors. Careful development and characterization of these materials and their welds is needed to verify the structural integrity of large-scale multicomponent structures. Understanding the local deformation behavior in heterogeneous materials and the mechanisms involved is key to further improve the performance and reliability of the materials at the global scale and can help in developing more accurate models and design rules. The full-field 3D digital image correlation (3D-DIC) technique was used to characterize two 316L multi-pass welds, based on cylindrical uniaxial tensile tests at room temperature, 350 °C, and 450 °C. The results were compared to solution annealed 316L material. The inhomogeneous character and dynamic behavior of the 316L base and weld materials were successfully characterized using 3D-DIC data, yielding high-quality and accurate local strain calculations for geometrically challenging conditions. The difference in character of the dynamic strain aging (DSA) effect present in base and weld materials was identified, where local inhomogeneous straining in weld material resulted in discontinuous type A Portevin–Le Châtelier (PLC) bands. This technique characterized the difference between local and global material behavior, whereas standard mechanical tests could not.

Keywords: 3D-DIC; 316L; multi-pass welds; dynamic strain aging; PLC effect

1. Introduction

Austenitic stainless steels similar to AISI 316L are widely used structural materials in currently existing nuclear reactors and in future generation IV reactors. To build large structural components (piping and internal structures of nuclear power plants, vessels of Gen IV reactors, etc.), multiple parts have to be joined together by welding. It is commonly acknowledged that welds can act as the weakest link; therefore, careful development, characterization, and understanding of the material and its welds are essential in order to ensure the structural integrity of such large-scale multicomponent structures.

In addition to the classical information gathered from mechanical testing, digital image correlation (DIC) [1,2] can provide valuable information about local strain fields and mechanical properties. Additionally, the DIC data can bridge the gap between experiments and simulations for modeling purposes. When studying surfaces that exist or move in the out-of-plane direction (curved surfaces or large out-of-plane deformations), a 3D correlation with two cameras in stereo vision (3D-DIC) is more appropriate to avoid in-plane strain errors [3] than a 2D correlation using only one camera that yields only in-plane information [4]. The information obtained from such experiments include local full-field surface displacement and multiaxial (in-plane) strain data, adding to the standard mechanical tests that only give the average uniaxial engineering strain values in the loading direction. The DIC technique can, therefore, be especially useful for nonhomogeneous

materials such as welds or when other nonuniform straining effects such as dynamic strain aging (DSA) occur [5–10].

DSA is a dynamic strengthening effect, and it is widely known that materials can show serrated flow curves at specific temperature and strain rate regimes, also known as the Portevin–Le Châtelier (PLC) effect or jerky flow [8,11–18]. The occurrence and intensity of this effect depend on the temperature, strain rate, chemical composition, and grain size [13,16,18–22]. On a microscopic scale, the PLC effect is a manifestation of DSA, where a constant competition exists between the motion of dislocations on the one hand (determined by temperature and strain rate) and the velocity of the diffusion of solute atoms (C and N) toward those dislocations (determined by temperature), pinning them in place on the other hand [15]. The pinning of these dislocations locally strengthens the material, and a certain critical stress is required to unpin them again. On a macroscopic scale, this process introduces bands or bursts of localized straining that move through the material, also called PLC bands. DSA has been known and studied at length for different materials. It is known to occur in austenitic stainless steels [10,12,18,20,23–25]. Commonly, three types of DSA behavior (type A, B and C) are described in the literature [8,10,11,16,23,25–28]. A type A serration is described as an abrupt rise and drop in the stress level around the general stress level. It is related to a PLC band, which nucleates and propagates continuously through the full material or test specimen. It usually nucleates at the shoulders of the specimen's gauge. Type B serrations are recognized by stress levels oscillating around the general stress level and are related to a PLC band appearing and propagating in a random manner. Type C serrations correspond to abrupt drops below the flow curve and are attributed to PLC bands that appear at random, without further propagation. The dynamic behavior of the PLC bands in base materials was previously investigated by DIC [8,10,28–31]. For welded materials, serrations related to DSA, superimposed on the engineering stress–strain curves, have been observed [21,24].

This work extends the investigations on weld material, to allow for a deeper insight into and understanding of the underlying mechanisms of this effect, bearing in mind the intrinsic nature of multi-pass welds comprising a variety of heterogeneous microstructures. Using a full-field technique such as DIC allows looking at the local and dynamic behavior of PLC bands in weld metal, in order to investigate how these PLC bands form and propagate in weld metal on a local scale. In this work, 3D-DIC investigations on uniaxial tensile tests of two types of 316L welds are performed on cylindrical specimens in the PLC temperature and strain rate regime. Miniature specimens are needed due to the limited availability of weld material, which makes it more challenging. In order to show the differences in dynamic behavior, the gained results from welds are compared with solution annealed 316L material.

2. Materials and Methods

Two austenitic stainless steel plates of solution annealed 316L (a 75 mm and a 32 mm thick plate) were multi-pass welded (submerged arc-welded (SAW) and gas tungsten arc-welded (GTAW), respectively), using a 316L filler material. The chemical compositions of both welds and the used reference 316L base material were measured by optical emission spectroscopy (OES) with a Spectro-SPECTROMAXx metal analyzer (Spectro Ametek, Kleve, Germany) and are listed in Table 1.

The samples had a reduced parallel section length of 12.0 mm and a gauge diameter of 2.4 mm, and they were extracted from the base material of the 75 mm plate (BM) and from the weld materials (WM1 and WM2 from the SAW and GTAW plates, respectively), as illustrated in the schematic in Figure 1. The figure also includes a macrograph of the welds, etched with Carpenter 300 series etchant and illustrative scanning electron microscope (SEM) images of the materials. It should be noted that the microstructure of material in the fusion zone is highly dependent on the location within the weld. Slow strain rate tensile (SSRT) tests were conducted in air at different temperatures (RT, 350 °C, and 450 °C) and with a strain rate of 5×10^{-5} s^{-1}. The test matrix of this work is given in Table 2. One

test (Test B) was performed on a specimen extracted in the T-orientation, while all other tests were performed on specimens extracted in the L-orientation. This was due to material availability, after disqualifying a few tests of L-oriented specimen performed at 350 °C. This information is given for completeness and should not influence the obtained results. The engineering stress–strain curves presented in this work were calculated on the basis of the load–line displacement, the load signal obtained from a hydraulic INSTRON 8810 testing machine (Instron, Norwood, MA, USA), and the initial parallel section length and cross-sectional area of the specimens, measured prior to testing.

Table 1. Chemical composition of the materials used in this work, as measured by OES (in wt.%).

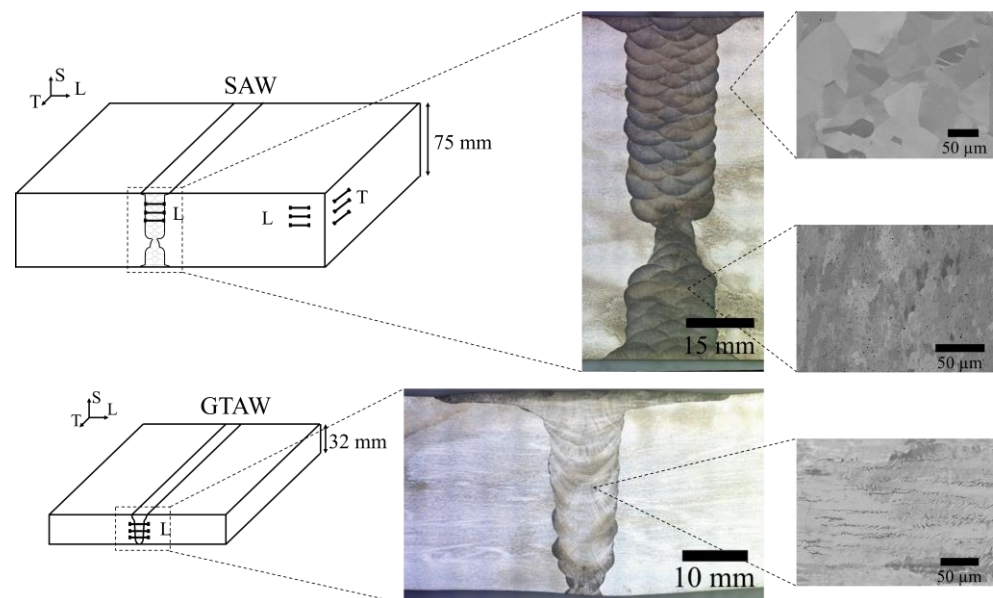|	C	Si	Mn	P	S	Cr	Mo	Ni	Al	N	Fe
BM (316L)	0.028	0.44	1.69	0.020	0.004	17.1	2.39	12.1	0.033	0.07	Bal.
WM1 (SAW)	0.020	0.52	1.43	0.018	0.008	18.9	2.47	12.2	0.023	0.05	Bal.
WM2 (GTAW)	0.018	0.45	1.65	0.027	0.017	18.1	2.54	12.1	<0.001	0.04	Bal.

Figure 1. Schematic drawing of the 75 mm thick SAW plate and the 32 mm thick GTAW plate (**left**) with the optical image of the macrograph etched by Carpenter 300 series etchant (**middle**) and SEM image of microstructures (**right**). The locations and orientations of extracted tensile samples are indicated. The relative sizes of the samples with respect to the size of the weld and plate thickness are correct.

A speckle pattern was manually applied on the specimen's surface using spray paint. To ensure good adhesion of the paint to the sample, even at elevated temperatures, high-temperature paints were used. The commercially available VHT flame-proof spray paints in black (SP102) and white (SP101) were used [29]. An example of a successfully applied speckle pattern on a round tensile specimen (Test A) is shown in Figure 2a. The pattern is uniform and has finely dispersed speckles, with an approximately 50–50 balance of black and white features. The mechanical tests were performed on an INSTRON 8810 machine, equipped with a custom-made forced convection furnace that allows the application of 3D-DIC at elevated temperatures. In order to minimize optical errors, the furnace is equipped with high-quality windows (parallel) to ensure a distortion-free view on the sample surface. Illumination happens through an additional separate window. A blue

light is mounted centrally above the cameras, to illuminate the sample while not letting the heated air created by the light interfere with the images taken by the cameras. Two horizontally aligned 8.9 MP 12-bit monochrome ADC camera sensors, which each record a 4096 × 2160 pixel image, were used for the 3D-DIC measurements. The positioning of the camera setup was optimized within the possible geometric boundaries of the tensile machine, furnace, desired magnification, and region of interest (ROI). A lens train with an Apo-Rodagon N105 lens and an extension tube of 108 mm was used for both cameras. With an aperture of F/16 and an approximate distance between a specimen and lens of 30 cm, this results in an estimated physical pixel size of 3.45 μm and an estimated depth of field of 0.75 mm, according to the lens selection software MachVis v5, provided by Correlated Solutions. Pictures of the complete setup are shown in Figure 2b. To ensure correct calibration, the setup was recalibrated before each test. A standard glass calibration grid with grid spacing of 0.89 mm was used and was placed inside of the furnace at the location where the specimen was positioned during testing. The calibration was performed at room temperature for all tests. The calibration grid was moved within the ROI and rotated at each of these positions around different axes (around the horizontal axis, around the vertical axis, and back and forth toward the central position between cameras). In the case of tests at high temperature, the performed room temperature calibration was verified at elevated temperature. On the basis of the correlation of few static images of the speckle pattern on the specimen, it was verified that the calculated projection error was still at an acceptable level. Example values for the calibration parameters of the setup are shown in Table 3. Only radial distortions of first order were allowed, and no skew, complex distortion, or high-magnification settings (which would force the central point of the calibration model on the central points of the cameras) were necessary to obtain a good-quality calibration, in correspondence with the physical dimensions of the setup. The intrinsic parameters for each individual camera include the image center, focal length of the lens, lens distortions correction parameter κ_1 for first-order correction, and average magnification. The extrinsic parameters define the relative orientation between the cameras and the specimen in angular values (α, β, and γ) and in translational values (T_x, T_y, and T_z). Of main interest is the stereo-angle β (indicated in Figure 2b), while the angles α and γ should be close to zero. The baseline represents the distance between both cameras.

Table 2. Test matrix of SSRT tests presented in this work.

	Plate/Material	Material Short Name	Orientation	Test Temperature (°C)
Test A	75 mm base	BM	L	22
Test B	75 mm base	BM	T	350
Test C	75 mm base	BM	L	450
Test D	75 mm SAW	WM1	L	22
Test E	75 mm SAW	WM1	L	350
Test F	75 mm SAW	WM1	L	350
Test G	75 mm SAW	WM1	L	450
Test H	75 mm SAW	WM1	L	450
Test I	32 mm GTAW	WM2	L	350
Test J	32 mm GTAW	WM2	L	350
Test K	32 mm GTAW	WM2	L	450
Test L	32 mm GTAW	WM2	L	450

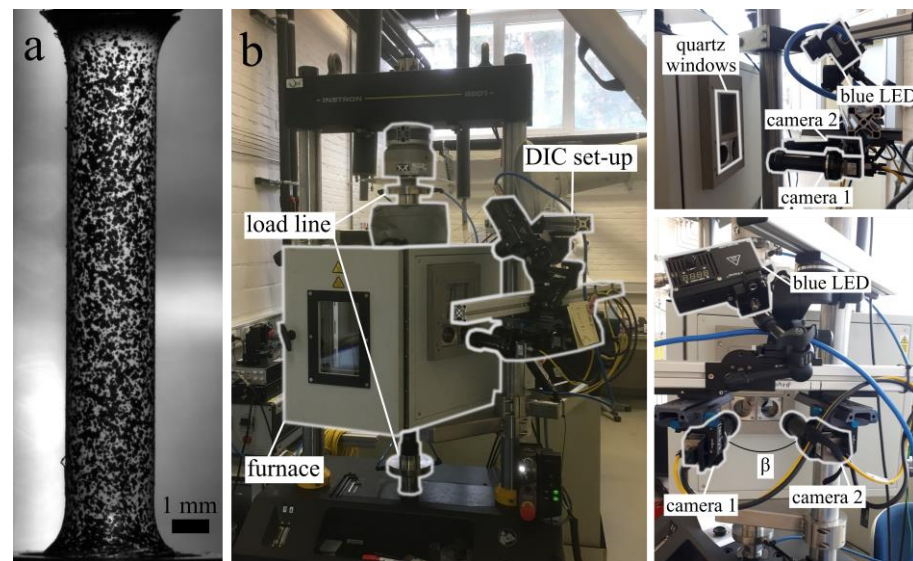**Figure 2.** (**a**) Example of speckle pattern. (**b**) Pictures of INSTRON machine used in this work with the customized forced convection oven and the 3D-DIC camera setup. The stereo-angle β is indicated.

Table 3. Values of intrinsic and extrinsic calibration parameters obtained for Test E.

	Intrinsic Camera 1	Intrinsic Camera 2		Extrinsic
Center (pixels)	1357.98 × 1910.88	997.966 × 1946.72	α (°)	−0.135801
Focal length x (pixel)	45,863.4	46,039	β (°)	19.8786
Focal length y (pixel)	45,863.4	46,039	γ (°)	−0.4268
κ_1	−0.0318309	0.0184563	T_x (mm)	−109.36
Avg. mag. (pixel/mm)	139.461	142.291	T_y (mm)	−0.213891
-	-	-	T_z (mm)	13.6092
-	-	-	Baseline (mm)	110.203

To reduce the disturbing influence of hot air between the sample and the cameras, the exposure time was tuned. An exposure time between 750 ms and 900 ms (equal for both cameras) was found to lead to a satisfactory tradeoff between the reduction in spatial resolution due to motion of the specimen during longer exposure time and the reduction in artificial motion of the speckle pattern due to the heat-induced movement of air in cases of a shorter exposure time. The accumulated average displacement during this longer exposure time was only 0.08 pixels. The exact exposure time for each individual test was selected according to the environmental conditions such as time of day or year, to avoid overexposure of the specimen. Load values from the INSTRON machine were recorded directly by the DIC setup, ensuring synchronized data.

The dedicated commercial Vic-3D 9 software supplied by Correlated Solutions was used to calculate the correlation of the images. The key postprocessing parameters include the subset size, the step size, the filter size (or strain window), and the choice of the reference image (always use the first image or incrementally adjusted reference image). The selection procedure of these parameters is explained in Appendix A, and the values are listed in Table 4.

The setting of incremental correlation (where the reference image is continuously updated to be the previously analyzed image) was chosen, as this is necessary due to the large degree of deformation in the investigated materials. In the case of such large deformation, using the initial image as the reference image would lead to incomplete correlation of the ROI and holes in the calculated displacement field. This results in biased strain calculations, since strain should be calculated on the basis of the full displacement environment around a discrete point. The drawback of incremental correlation is that any

error present in previously correlated images is taken along to the next one and is, therefore, summed for all images. On the other hand, correlating an image with the initial image as the reference image will have an intrinsically higher error value, in the case of large deformation, when the first-order approach of subset fitting loses its validity. It was found in the current case that the difference in first principal strain e_1 values between incremental and non-incremental correlation was negligible, while the values obtained by incremental correlation gave a complete correlation over the full field, without missing data points.

Table 4. Selected postprocessing parameters used for all tests analyzed in this work, based on VSG study performed on Test D.

Parameter	Value
Subset size (pixels)	81
Step size (pixels)	10
Filter size (nodes)	9

The noise floor on the strain (see Appendix A for more information) was calculated for each test individually, for the selected postprocessing parameters, and is given in Table 5, together with the calculated mechanical properties of all tests presented in this work and the frequency of images used for each correlation. Higher values of the noise floor were found for tests at elevated temperatures. This is expected from the remaining influence of the disturbing influence of hot air between the sample and the cameras.

Table 5. Tests results, noise-floor and time resolution for all tests presented in this work.

	Test Results				3D-DIC	
	Rp0.2 MPa	Rm MPa	UE (−)	TE (−)	Noise-Floor ($\mu\epsilon$)	Frequency of Images
Test A	280	603	0.52	0.66	35	1 every 30 s
Test B	191	467	0.33	0.43	624	1 every 30 s
Test C	238	461	0.32	0.42	236	1 every 30 s
Test D	472	585	0.18	0.27	30	1 every 20 s
Test E	385	481	0.11	0.18	95	1 every 20 s
Test F	386	479	0.11	0.18	77	1 every 20 s
Test G	376	474	0.11	0.17	145	1 every 20 s
Test H	365	461	0.09	0.15	327	1 every 20 s
Test I	347	469	0.12	0.19	175	1 every 30 s
Test J	345	471	0.13	0.20	107	1 every 20 s
Test K	287	450	0.16	0.22	316	1 every 30 s
Test L	318	453	0.12	0.20	575	1 every 30 s

To show strain localization and development, maps with the strain rate as a function of time were used. As illustrated in Figure 3, the value of the time derivative of the component of the strain in the loading direction (dE_{yy}/dt) was interpolated from the correlated data at 200 equidistant points along the central line on the specimen surface in that direction, and this was performed for all correlated frames. The extracted values along the line for each image were subsequently plotted in the x-direction on a color plot, such that the x-axis represents time (or equivalently in a displacement-controlled test, engineering strain) and the y-axis corresponds to the position in the loading direction on the initial sample surface. Using this way of visualization, all information of one test can be shown in one overview graphic, representing the dynamic behavior of the full test. In addition, this allows identifying the localization of strain on the original sample surface. This method to extract and visualize the data is schematically shown in Figure 3.
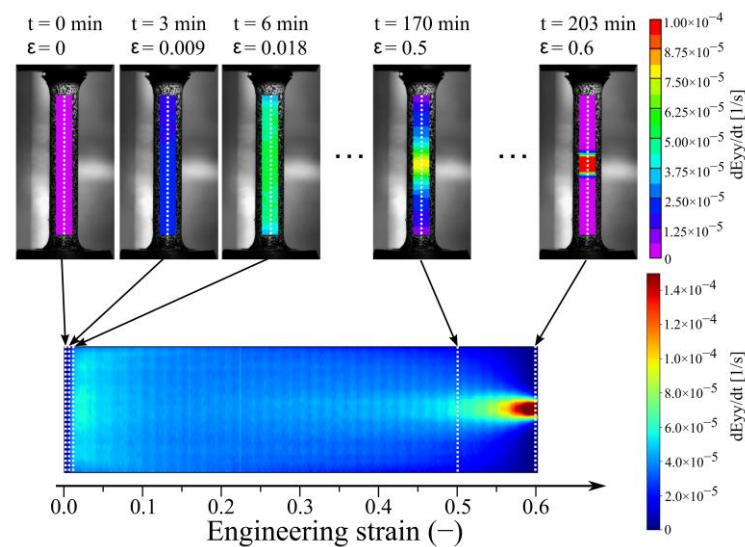
Figure 3. Illustration of data extraction procedure for strain rate maps. Strain rate values are interpolated and extracted at 200 equidistant points along the central line in the loading direction on the sample surface (dotted lines) on each of the individual time frames. The extracted strain rate values for each timeframe are subsequently plotted in a color map, horizontally next to each other, as a function of time or, equivalently, in a displacement-controlled test, engineering strain.

3. Results

In Figure 4, strain rate maps of tests performed on the base material are shown. The maps of a test performed at room temperature (Test A), at 350 °C (Test B), and at 450 °C (Test C) are overlaid with the engineering stress–strain curves in white on each map for illustrative purposes. DSA and the associated PLC bands occurred in the material at elevated temperatures. Although visible (but not clearly) on the stress–strain curve alone, in combination with DIC, four clear localized PLC bands moving up and halfway down through the sample near the end of the test between 0.25 and 0.35 engineering strain could be identified in the test performed at 350 °C (Test B in Figure 4). For the test at 450 °C (Test C in Figure 4), the localized strain bands were more prominent and occurred with a higher frequency on the strain rate maps, already distinguishable from 0.04 engineering strain, and also clearly observable on the stress–strain curves. The frequency of the PLC bands coincided with the frequency of the serrations on the stress–strain curve, which decreased toward the end of the test. The bands observed in these two tests with continuous movement over the full gage section could be related to type A PLC bands, according to the description in literature, as discussed before. This temperature- and strain rate-dependent effect was not observed in the base material at room temperature (Test A in Figure 3).

For the test performed on WM1 at room temperature (Test D in Figure 5), the difference between base and weld metal becomes clear. While the straining in the sample of the base material was fairly homogeneous, this was not the case for the weld metal test. Immediate localization of the straining occurred after passing the yielding point, indicating three distinct weaker zones in this specific specimen, and confirming the pronounced effect of weld heterogeneity on the specimen's deformation behavior. The tests at elevated temperatures showed a noisier image; however, the different weaker zones could still be identified. On the WM1 tests performed at 350 °C (Test E and Test F in Figure 5), indications of a rapid change in straining location can be seen in the strain rate map at engineering strain values between 0.07 and 0.12 for Test E and between 0.10 and 0.12 for Test F. The two tests performed at 450 °C on the WM1 material (Test G and Test H in Figure 5) had more pronounced serrations on the stress–strain curves, and the strain rate maps showed a similar but stronger discontinuous effect, as was present for 350 °C. The PLC bands were observed on the strain rate maps at an engineering strain between 0.04 and 0.12 for Test G and between 0.06 and 0.11 for Test H. Even though the rapid change in straining location

in these tests resembled the type A PLC bands in the base material tests (moving up and down the specimen), it had a discontinuous nature. In addition, the discrete locations, where the straining fluctuated, represent the already weaker zones in the previous part of the test and, therefore, had a higher degree of accumulated plastic deformation in the microstructure of the material.
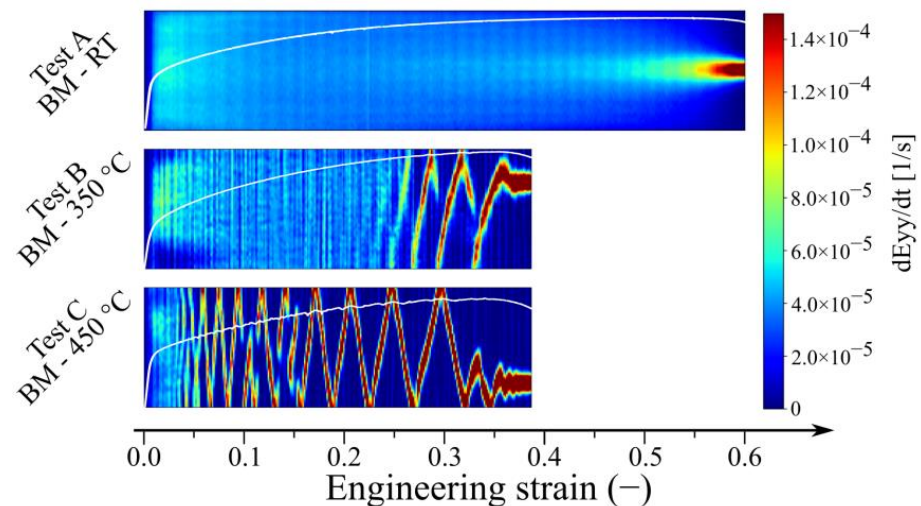

Figure 4. Strain rate maps of tests performed on base material at RT (Test A), at 350 °C (Test B), and at 450 °C (Test C). The engineering stress–strain curves of each test are overlaid on the strain rate maps in white.

Similar maps are shown in Figures 5 and 6 for tests performed on the SAW weld material (WM1) and the GTAW weld material (WM2), respectively.
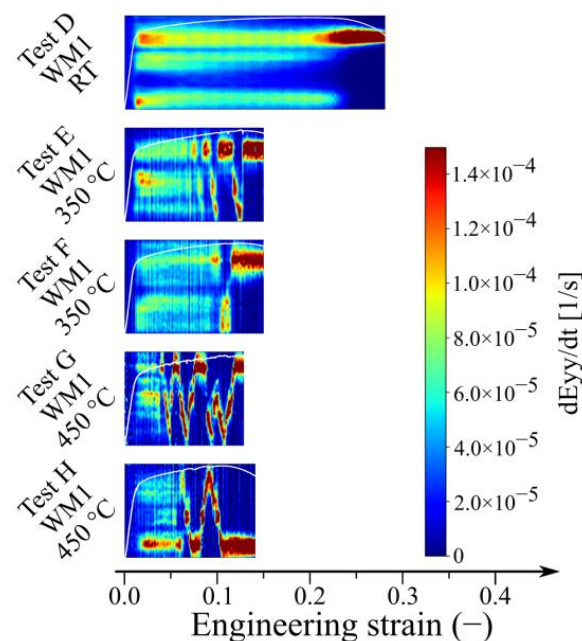

Figure 5. Strain rate maps of tests performed on the SAW material (WM1) at RT (Test D), at 350 °C (Test E and F) and at 450 °C (Test G and H). The engineering stress–strain curves of each test are overlaid on the strain rate maps in white.
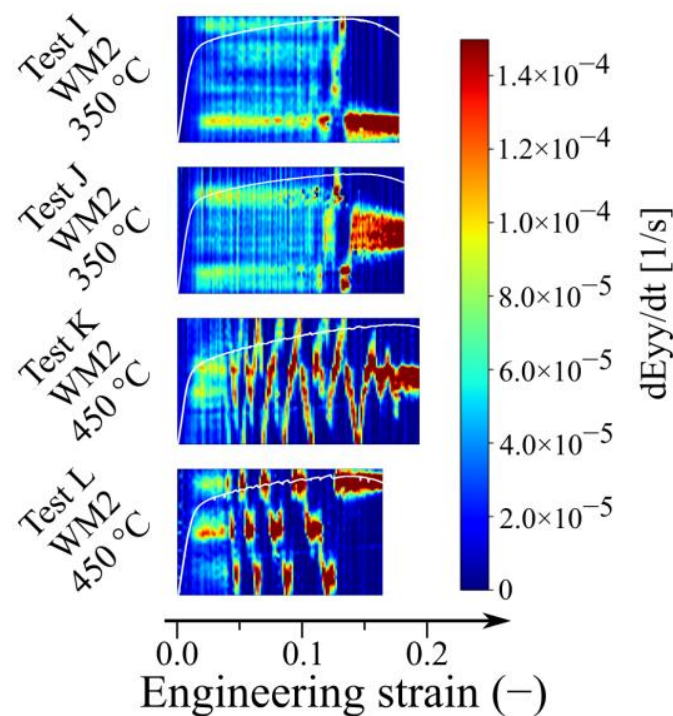
Figure 6. Strain rate maps of tests performed on the GTAW material (WM2) at 350 °C (Test I and J) and at 450 °C (Test K and L). The engineering stress–strain curves of each test are overlaid on the strain rate maps in white.

Similar behavior was observed in the GTAW material (WM2), illustrated in Figure 6. Test I and Test J, which were performed at 350 °C, showed quick and discrete changes in straining location near the end of the tests, between an engineering strain of 0.12 and 0.14 for Test I and between 0.11 and 0.14 for Test J. This strain range increased at 450 °C, where PLC bands were present between an engineering strain of 0.04 and 0.18 for Test K and between 0.04 and 0.13 for Test L. A more continuous motion of the PLC bands was observed in the strain rate map of Test K than in the map of Test L.

To get a closer look on the shape of the serrations superimposed on the stress–strain curves, Figure 7 shows a section of each of the stress–strain curves of tests at elevated temperatures presented in Figures 4–6. The curves are plotted with an offset but with an identical scale, for both the strain and the stress values. In this way, the amplitudes and frequencies of the serrations could be directly compared between tests. It is clear that all tests performed at 350 °C (Test B, Test E, Test F, Test I, and Test J) had a smaller serration amplitude than the tests performed at 450 °C (Test C, Test G, Test H, Test K, and Test L). For the tests at 350 °C, even in this enlarged representation, the serrations had a small amplitude and were hard to detect on top of the instrumental noise. At 450 °C, clearly visible serrations could be seen. Although they were very irregular, most serrations were similar to the type A serrations, where the stress increased, followed by a decrease in stress, relative to the general stress–strain trend. In addition to the type A serrations, a few sharp drops in stress values were observed (Tests C, E, G, and L), along with minor oscillations superimposed on the curves. These features may have been artefacts of the experimental setup; however, it was not possible to investigate these more deeply. In principle, the shape of these oscillations and sharp drops resembled the type B and type C serrations as described in the literature; however, this was not confirmed by the DIC data.
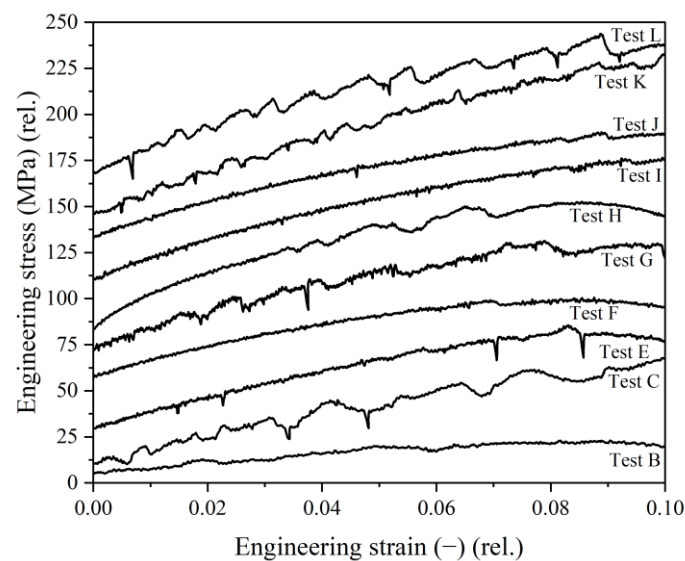
Figure 7. Comparison of serrated sections of engineering stress–strain curves of all tests performed at elevated temperatures. The stress and strain scales were identical for all tests, in order to be able to compare serration amplitudes and frequencies.

4. Discussion

The serrated flow curves in 316L-type base materials are a manifestation of the DSA effect, where the pinning of dislocations by solute atoms temporarily strengthens the material. This was observed for the tests performed at 350 °C (Test B) and 450 °C (Test C) of the base material in Figure 4. This is in agreement with what is found in austenitic stainless steel materials in the literature, based on both the shape and the size of the serrations imposed on the stress–strain curve alone [19,20,23,25], as well as based on full-field data obtained by techniques such as DIC [8,10]. The test at room temperature (Test A in Figure 4) was an example of a typical uniaxial tensile test with a uniform strain field, which narrowed more and more toward the central part, and where necking started at the UTS point. No DSA or PLC bands were present in the test, which agrees with literature. For instance, the effect was reported in 316L(N) at temperatures between 250 °C and 600 °C at strain rates of $3.16 \times 10^{-5} \text{ s}^{-1}$ [19].

At elevated temperature, the application of the full-field DIC technique was proven to be more sensitive (or even essential) for the registration and characterization of PLC bands. It allowed visualization of the PLC bands in the strain rate maps. It is important to emphasize that, even when there were only slight or no serrations distinguishable from the noise on the engineering stress–strain curves, e.g., the case in Test B illustrated in Figures 4 and 7, DIC could confirm the presence of PLC bands. Additionally, the technique allowed for better characterization of the type of DSA behavior. The serrations on the stress–strain curves of Test B and Test C (Figure 7) did not clearly show the typical type A behavior described in the literature, i.e., separated instances of an abrupt rise in strength, followed by a drop below the general level of the stress–strain curve, later to rise again toward the general level. However, the DIC data of these tests (Figure 4) suggested the continuously moving type A PLC bands.

On the contrary, for the tests performed on weld material at elevated temperatures (Figures 5 and 6), the motion of the PLC bands had a discontinuous nature. The PLC bands jumped between positions where previous straining already occurred in the beginning of the test. It should be noted that, even though the description of a type B PLC band as a moving band which initiates at randomly changing locations at first sight seems to match the observed behavior in all welded tests (Figures 5 and 6), the observed behavior was fundamentally different. This became clear when comparing the results of the weld metal tests at elevated temperatures in this work with, for example, the type B bands

presented in [10], where Lee et al. indeed observed that the nucleation of type B PLC bands occurred at seemingly random positions throughout the specimen gauge section. While the concept of type B behavior is related to the discontinuous behavior of the band in an initially homogeneous material, the results in the weld metal at elevated temperatures presented here were actually related to a continuous band behavior (type A) in an initially inhomogeneous material (weld metal). Describing the DSA in the weld material tests presented in this work as such was confirmed after looking at the scatter between different tests; during parts of some tests (e.g., Test G, Test H, or Test K), the PLC band even moved in a continuous manner.

The propagation or the occurrence of a PLC band in a specific position in the material is related to the local microstructure and the degree of deformation already accumulated during the test. The difference in behavior between the base and weld material tests at high temperature showed that the DSA effect in the investigated materials was restricted to the locations with enough dislocations present due to previous straining, such that the solute atoms could pin those in place. This locally and temporarily strengthened the material. For the base material, the full gauge section of the test specimen was initially deformed uniformly, resulting in the continuous movement of the PLC band up and down through the full sample. In the weld material, only the initially weaker parts of the sample that were previously deformed had a high enough dislocation density for the effect to take place. Other previously nondeformed locations would not participate in the DSA, as these did not reach the critical (true) strain. This resulted in the discontinuous movement of the PLC bands over the sample. In addition, this implies that only a part of the weld material was actively used and deformed during testing the sample.

The literature shows that the DSA effect also influences the mechanical properties of materials and is characterized by peaks in flow strength, loss of ductility and toughness, and a negative strain rate sensitivity [21,32,33]. It is, therefore, important to know the temperature and strain rate regions where DSA occurs in a structural material when using it for engineering purposes. DIC has been proven to greatly increase the amount of information that can be gained from tensile tests compared to purely using stress–strain curves. It has been shown that the technique allows determining the DSA temperature and strain rate regions with a higher sensitivity. In addition, in engineering applications, different geometrical features such as holes, edges, or notches imply certain strain rate gradients that make the material more sensitive to the PLC effect and DSA [30]. The weld material itself also seemed more susceptible to DSA and the PLC effect, due to its heterogeneous characteristic and consequently induced strain rate gradients across the material.

5. Conclusions

In this work, the deformation behavior of 316L base and weld material at different temperatures was investigated. DIC was shown to be an effective technique to characterize the local deformation behavior of complex materials such as welds. The technique was more sensitive (and for some tests crucial) for observing PLC bands directly on the specimen surface, compared to if only the size and shape of the serrated stress response on the stress–strain curves was recorded. In case of serrations with low amplitudes, this was difficult to distinguish from noise. In addition, in contrast to what is presented in the literature, the different types of PLC bands were not easily distinguished on the basis of stress–strain behavior alone, and the DIC data performed better in this regard. In the temperature and strain rate regimes tested in this work, type A PLC bands, identified by DIC, moved continuously through the homogeneous base material. In the case of heterogeneous materials such as welds, due to the heterogeneous deformation during the initial stage of the mechanical tests at high temperature, type A PLC bands moved in a discontinuous way through the material. The type A PLC bands moved only through regions with a sufficient dislocation density, resulting in an apparent discontinuous motion, in contrast to the continuous way in which they moved in homogeneously deformed

base material. The weld material itself seemed more susceptible to DSA and the PLC effect, due to its heterogeneous character and consequently induced strain rate gradients across the material. In general, the DIC technique can be used to observe the local variations in mechanical properties in heterogeneous materials such as welded materials. By using the DIC technique, the difference between local and global material behavior can be characterized, whereas the standard mechanical tests were unable to distinguish this difference.

Author Contributions: Conceptualization, A.L. and E.S.; methodology, A.L.; software, A.L.; validation, E.S., S.H., J.L. and R.H.P.; formal analysis, A.L.; investigation, A.L.; resources, E.S.; data curation, A.L.; writing—original draft preparation, A.L.; writing—review and editing, E.S., J.L., S.H. and R.H.P.; visualization, A.L.; supervision, E.S., S.H. and R.H.P.; project administration, E.S.; funding acquisition, E.S. All authors have read and agreed to the published version of the manuscript.

Data Availability Statement: The raw/processed data required to reproduce these findings cannot be shared at this time as the data also form part of an ongoing study.

Conflicts of Interest: The authors declare no conflict of interest.

Appendix A

The key postprocessing parameters for DIC analysis include the subset size, the step size, the filter size (or strain window), and the choice of the reference image (always use the first image or incrementally adjusted reference image). Using those parameters, the spatial resolution (SR) and the virtual strain gage (VSG) size can be determined, and the noise floor on the strain can be measured. The speckle feature size is already fixed by the application of the paint and magnification of the lensing system when the test data are at hand, and it puts a lower limit to the possible subset size to be used, so that at least the suggested number of three speckle features is present in a subset [1,2]. A larger subset size increases the calculation time and increases the spatial smoothing, but also decreases the noise and improves the accuracy to a certain limit [34]. The step size represents the distance (in pixels) between the different nodes for calculating the different quantities. Smaller step sizes will, to a certain extent, increase the spatial resolution. However, decreasing the step size to lower than one-third of the subset size does not yield more spatial information, while increasing calculation time, but it could be useful to better capture the exact locations of extrema. Since strain is a derivative quantity, the strain values are calculated on the basis of the environment around a particular node. This can result in very noisy data; therefore, the Vic-3D software applies a Gaussian smoothing filter on the strain data, according to the filter size (in number of nodes). A Gaussian filter with a cutoff at 90% decay at the filter size is applied on the strain values [35]. Careful selection of this filter size is necessary, since noise can be amplified when numerical differentiation is applied [36]. As a rule of thumb, the filter size multiplied by the step size should be larger than the subset size. For practical reasons, since the geometry of the specimens is long but narrow, the filter size multiplied by the step size should also be significantly smaller than the width of the ROI, which was approximately 300 pixels in the tests under consideration.

Following the suggestions of Reu [37], a VSG size study to determine the optimal values of these postprocessing parameters was performed on the test showing the highest gradients of deformation present (Test D). Subset sizes between 41 and 101 pixels were explored, along with step sizes between five and 15 pixels and filter sizes between five and 21 nodes, depending on the used step size and limitations discussed before. For this

study, three images (reference image, undeformed image, and image with highest strain gradients) were selected, and the VSG size was determined by

$$VSG = ((SW - 1) \cdot ST) + 1, \tag{A1}$$

while the SR was determined by

$$SR = ((SW - 1) \cdot ST) + SS, \tag{A2}$$

where SW is the strain window or filter size, ST is the step size, and SS is the subset size used for the correlation. The strain values were extracted along a line, both on the undeformed image and on the image with the highest strain gradients, intersecting the region with the highest strain value and gradient. The noise floor on the strain values was calculated by determining the standard deviation on the strain values extracted from the undeformed image, where no strain is present. The optimal parameters were selected by optimizing the SR and VSG size, while making sure that the largest gradients of the strain were still captured in the correlation results. On the basis of the concept of convergence (where a smaller value for VSG size did not increase peak values of strain [37]), the postprocessing parameters were selected (Table 4). The optimized parameters based on this VSG size study of Test D were used for all tests, as the speckle patterns applied were similar in shape, the setup of the test system and sample geometry were the same, and Test D had the highest strain gradients. It should be noted, however, that the noise floor was test-dependent.

References

1. Orteu, J.J.; Schreier, H.; Sutton, M.A. *Image Correlation for Shape, Motion and Deformation Measurements*; Springer: Berlin/Heidelberg, Germany, 2009.
2. Jones, E.M.C.; Iadicola, M.A. *A Good Practices Guide for Digital Image Correlation*; International Digital Image Correlation Society, 2018. Available online: https://idics.org/guide/ (accessed on 14 January 2023).
3. Sutton, M.A.; Yan, J.H.; Tiwari, V.; Schreier, H.W.; Orteu, J.J. The effect of out-of-plane motion on 2D and 3D digital image correlation measurements. *Opt. Lasers Eng.* **2008**, *46*, 746–757. [CrossRef]
4. Pan, B.; Xie, H.; Wang, Z.; Qian, K.; Wang, Z. Study on subset size selection in digital image correlation for speckle patterns. *Opt. Express* **2008**, *16*, 7037. [CrossRef]
5. Ramachandran, S.; Lakshminarayanan, A.K.; Reed, P.A.S.; Dulieu-Barton, J.M. Application of imaging techniques to determine the post-yield behaviour of the heterogeneous microstructure of friction stir welds. *Exp. Mech.* **2021**, *61*, 1045–1063. [CrossRef]
6. Midawi, A.R.H.; Biro, E.; Kistampally, S. Effect of coating and welding wire composition on AHSS GMA welds. *Weld. J.* **2021**, *100*, 396–409. [CrossRef]
7. Hertelé, S.; Gerven, F.V.; Naib, S.; Gubeljak, N.; De Waele, W. Experimental and numerical slip line analysis of welded single-edge notched tension specimens. *Procedia Struct. Integr.* **2016**, *2*, 1763–1770. [CrossRef]
8. Zavattieri, P.D.; Savic, V.; Hector, L.G., Jr.; Fekete, J.R.; Tong, W.; Xuan, Y. Spatio-temporal characteristics of the Portevin–Le Châtelier effect in austenitic steel with twinning induced plasticity. *Int. J. Plast.* **2009**, *25*, 2298–2330. [CrossRef]
9. Luo, H.; Kang, G.; Kan, Q.; Huang, Y. Experimental investigation on the heterogeneous ratchetting of SUS301L stainless steel butt weld joint during uniaxial cyclic loading. *Int. J. Fatigue* **2017**, *105*, 169–179. [CrossRef]
10. Lee, S.-Y.; Takushima, C.; Hamada, J.-I.; Nakada, N. Macroscopic and microscopic characterizations of Portevin-Le Chatelier effect in austenitic stainless steel using high-temperature digital image correlation analysis. *Acta Mater.* **2021**, *205*, 116560. [CrossRef]
11. Ananthakrishna, G. Current theoretical approaches to collective behavior of dislocations. *Phys. Rep.* **2007**, *440*, 113–259. [CrossRef]
12. Pham, M.S.; Holdsworth, S.R. Dynamic strain ageing of AISI 316L during cyclic loading at 300 °C: Mechanism, evolution, and its effects. *Mater. Sci. Eng. A* **2012**, *556*, 122–133. [CrossRef]
13. Cai, M.C.; Niu, L.S.; Yu, T.; Shi, H.J.; Ma, X.F. Strain rate and temperature effects on the critical strain for Portevin–Le Chatelier effect. *Mater. Sci. Eng. A* **2010**, *527*, 5175–5180. [CrossRef]
14. Rodriguez, P. Serrated plastic flow. *Bull. Mater. Sci.* **1984**, *6*, 653–663. [CrossRef]
15. Cottrell, A.H.; Bilby, B.A. Dislocation theory of yielding and strain ageing of iron. *Proc. Phys. Soc. Sect. A* **1949**, *62*, 49–62. [CrossRef]
16. Brindley, B.J.; Worthington, P.J. Yield-point phenomena in substitutional alloys. *Metall. Rev.* **1970**, *15*, 101–114. [CrossRef]
17. Pink, E.; Grinberg, A. Serrated flow in a ferritic stainless steel. *Mater. Sci. Eng.* **1981**, *51*, 1–8. [CrossRef]
18. Samuel, K.G.; Mannan, S.L.; Rodriguez, P. Serrated yielding in AISI 316 stainless steel. *Acta Metall.* **1988**, *36*, 2323–2327. [CrossRef]
19. Choudhary, B.K. Influence of strain rate and temperature on tensile deformation and fracture behavior of type 316L(N) austenitic stainless steel. *Metall. Mater. Trans. A* **2013**, *45*, 302–316. [CrossRef]

20. Hong, S.; Lee, S. The tensile and low-cycle fatigue behavior of cold worked 316L stainless steel: Influence of dynamic strain aging. *Int. J. Fatigue* **2004**, *26*, 899–910. [CrossRef]
21. Kim, K.C.; Kim, J.T.; Suk, J.I.; Sung, U.H.; Kwon, H.K. Influences of the dynamic strain aging on the J-R fracture characteristics of the ferritic steels for reactor coolant piping system. *Nucl. Eng. Des.* **2004**, *228*, 151–159. [CrossRef]
22. Samuel, K.G.; Gossmann, O.; Huthmann, H. Temperature dependence of fracture toughness (J-R-curves) of a modified type 316L austenitic stainless steel. *Int. J. Press. Vessel. Pip.* **1990**, *41*, 59–74. [CrossRef]
23. Kim, D.W.; Ryu, W.S.; Hong, J.H. Effect of nitrogen on the dynamic strain ageing behaviour of type 316L stainless steel. *J. Mater. Sci.* **1998**, *33*, 675–679. [CrossRef]
24. Muhamed, G.; Gündüz, S.; Erden, M.; Taştemur, D. Dynamic strain aging behaviour in AISI 316L austenitic stainless steel under as-received and as-welded conditions. *Metals* **2017**, *7*, 362. [CrossRef]
25. Choudhary, K. Activation energy for serrated flow in type 316L(N) austenitic stainless steel. *Mater. Sci. Eng. A* **2014**, *603*, 160–168. [CrossRef]
26. Hähner, P.; Ziegenbein, A.; Rizzi, E.; Neuhäuser, H. Spatiotemporal analysis of Portevin-Le Châtelier deformation bands: Theory, simulation, and experiment. *Phys. Rev. B* **2002**, *65*, 134109. [CrossRef]
27. Xiang, G.-F.; Zhang, Q.-C.; Liu, H.-W.; Jiang, H.-F.; Wu, X.-P. Deformation measurements of three types of Portevin-Le Chatelier bands. *Chin. Phys.* **2006**, *15*, 2378–2384.
28. Yuzbekova, D.; Mogucheva, A.; Borisova, Y.; Kaibyshev, R. On the mechanisms of nucleation and subsequent development of the PLC bands in an AlMg alloy. *J. Alloy. Compd.* **2021**, *868*, 159135. [CrossRef]
29. VHT Flameproof Coating: High Heat Coating. Available online: https://www.vhtpaint.com/high-heat/vht-flameproof-coating (accessed on 25 January 2023).
30. Ren, S.C.; Morgeneyer, T.F.; Mazière, M.; Forest, S.; Rousselier, G. Effect of Lüders and Portevin-Le Chatelier localization bands on plasticity and fracture of notched steel specimens studied by DIC and FE simulations. *Int. J. Plast.* **2021**, *136*, 102880. [CrossRef]
31. Lebyodkin, M.; Bougherira, Y.; Lebedkina, T.; Entemeyer, D. Scaling in the local strain-rate field during jerky flow in an Al-3%Mg alloy. *Metals* **2020**, *10*, 134. [CrossRef]
32. Wang, H.D.; Berdin, C.; Mazière, M.; Forest, S.; Prioul, C.; Parrot, A.; Le-Delliou, P. Experimental and numerical study of dynamic strain ageing and its relation to ductile fracture of a C-Mn steel. *Mater. Sci. Eng. A* **2012**, *547*, 19–31. [CrossRef]
33. Chakravartty, J.K.; Wadekar, S.L.; Sinha, T.K.; Asundi, M.K. Dynamic strain-ageing of A203D nuclear structural steel. *J. Nucl. Mater.* **1983**, *119*, 51–58. [CrossRef]
34. Pan, B.; Qian, K.; Xie, H.; Asundi, A. Two-dimensional digital image correlation for in-plane displacement and strain measurement: A review. *Meas. Sci. Technol.* **2009**, *20*, 062001. [CrossRef]
35. Correlated Solutions. Application Note—Strain Filter Selection. Available online: https://correlated.kayako.com/article/43-strain-filter-selection (accessed on 12 January 2023).
36. Rossi, M.; Lava, P.; Pierron, F.; Debruyne, D.; Sasso, M. Effect of DIC spatial resolution, noise and interpolation error on identification results with the VFM. *Strain* **2015**, *51*, 206–222. [CrossRef]
37. Reu, P. Virtual strain gage size study. *Exp. Tech.* **2015**, *39*, 1–3. [CrossRef]